ARTICLE

# Effects of Size and Microstructures on Infrared Spectra of Pyrolusites

Ruo-yu Cai[a], Wen-lou Wang[a*], Heng Jiang[a], Lei Shi[a], Bo He[b], Shi-qiang Wei[b]

*a. Department of Chemical Physics, University of Science and Technology of China, Hefei 230026, China*

*b. National Synchroton Radiation Laboratory, University of Science and Technology of China, Hefei 230029, China*

(Dated: Received on June 26, 2010; Accepted on January 9, 2011)

Nanofibrous pyrolusite ($\beta$-$MnO_2$) was synthesized. The particle shape changes from nanofibers to nanoparticles after grinding, and the phase structure does not change. The local environment around the central manganese ion has a slight change in nanoparticles related to nanofibers. Fourier transform infrared (FTIR) spectra showed that $A_{2u}$ mode frequency shifts from 514 $cm^{-1}$ to 574 $cm^{-1}$ to 617 $cm^{-1}$ gradually while the particle shape and size change from long nanofibers to short fibers and to nanoparticles. The extra vibrational band that is unpredicted by factor group analysis originates from the contribution of $A_{2u}$ mode of the particles with different sizes and shapes in the studied sample. On the basis of Rietveld refinement analysis of XRD profiles and the FTIR spectra, we think that two kinds of $MnO_6$ octahedral geometries, *i.e.*, 4 long+2 short and 4 short+2 long, could exist in pyrolusites synthesized by different route. The maximum vibrational frequency in the FTIR spectra of pyrolusites is sensitive to these micro-structures. Assignment of four vibrational bands in the middle and far infrared region has been made.

**Key words:** $\beta$-$MnO_2$, Fourier transform infrared spectrum, Microstructure

## I. INTRODUCTION

Manganese dioxides with tunnel and layered crystal structures offer distinctive properties and wide applications as catalysts, sieves, and electrode materials of batteries [1−3]. Pyrolusite ($\beta$-$MnO_2$), the most stable form among the tunnel-structured manganese dioxides, is often used as a model manganese oxide constructed by 1×1 tunnels [4, 5]. Pyrolusite has the tetragonal rutile-structure, which belongs to $D_{4h}^{14}$ spectroscopic group, involving two formula units per unit cell. Factor group analysis gives the following modes:

$$\Gamma = A_{1g}(R)+A_{2g}+A_{2u}(IR)+B_{1g}(R)+ B_{2g}(R)+2B_{1u}+E_g(R)+3E_u(IR)$$

Therefore, this oxide should present four vibrational active modes in infrared ($A_{2u}$+$3E_u$) and four in Raman ($A_{1g}$+$B_{1g}$+$B_{2g}$+$E_g$). However, the IR spectra of pyrolusite were seemly dependent on the sample source and the synthetic route [6−10]. Generally, there are two kinds of the infra-red (IR) spectra, one has four vibrational bands in the mid- and far-infrared region [6], and another has five [6, 7]. The latter is discordant with the theoretical prediction.

The origin of the extra vibrational band that is unpredicted by factor group analysis has not been revealed up to now although Potter and Rossman claimed that the resolution of three bands in the mid-infrared region improved as the increase of orthorhombic pyrolusite, an impure phase in natural pyrolusites [6]. The recent study made by Julien *et al.* excluded the effect of orthorhombic pyrolusite, the IR spectrum, in which five bands appeared, was recorded from pure tetragonal pyrolusite with well-crystalline [7].

Another unsolved question is what causes large variation in the IR spectra of pyrolusite in the mid-infrared region [6−10]. For example, Nilsen *et al.* [8], Julien *et al.* [7], and Tang *et al.* [9] reported the IR spectra of pyrolusite, in which the major bands were located at about 520 and 584 $cm^{-1}$ [8], 545 and 618 $cm^{-1}$, and 618 and 655 $cm^{-1}$, respectively. The large variation in the IR spectra of rutile-structured dioxides, such as $SnO_2$ and $TiO_2$, was contributed to the effect of particle shape and size [11−14]. Farmer suggested that shape may be the cause of large variations in the IR spectra of different powdered rutile samples [11]. Pyrolusite, which is isostructural rutile, should have a similar variation in the IR spectrum. However, Potter and Rossman concluded that particle shape was not responsible for the variation in pyrolusite IR spectra [6]. It is worth re-studying this issue in order to reveal the cause of variation in purolusite IR spectra.

The maximum frequency in the Fourier transform infrared (FTIR) spectra of pyrolusite is different [6−9]. The maximum frequency at about 650 $cm^{-1}$ was observed, whereas the band at about 720 $cm^{-1}$ appears in

*Author to whom correspondence should be addressed. E-mail: wlwang@ustc.edu.cn

 

the spectra reported by Potter and Rossman [6], Julien *et al.* [7], and Nilsen *et al.* [8]. Some researchers reported the spectra with the different maximum frequency in the same work, but they did not give any explanation [6, 8]. These two frequencies appear in the spectra of both natural samples [6] and synthetic samples [7−9], suggesting that this is a fundamental issue concerning micro-structure of pyrolusite.

It is well-known that the spectrum quality is dependent on the sample quality. The large single-crystal pyrolusite sample is scarcely obtained due to the unstablility of pyrolusite at higher temperature. Most of pyrolusite samples studied so far were powders with various defects and with irregular morphology. With the development of synthetic technique, well-crystallized manganese dioxides with various morphologies can be synthesized [15−17]. This supplies an opportunity to study vibrational feature of pyrolusite, and to study the nature of the variation in the IR spectrum.

In this work, we studied the FTIR spectrum of nanofibrous pyrolusite well-grown along *c* axis. In order to reveal the origin of the unpredicted vibrational band and the nature of the variation in the IR spectra, we also employed TEM (transmission electron microscope), SEM (scanning electron microscope), XRD (the powder X-ray diffraction), and XAFS (X-ray absorption fine structure) to study the morphology, the phase structure and the local environment in the samples before and after grinding.

## II. EXPERIMENTS

### A. Synthesis of precursor $CTAMnO_4$

A detailed description of the synthesis of $CTAMnO_4$ (cetyltrimethylammonium permanganate) can refer to Refs.[18, 19]. The equimolar $KMnO_4$ and CTAB (cetyltrimethylammonium bromide) solutions were prepared in beakers. Purple gel was rapidly formed after mixing both solutions by means of ultrasonication. The gel was aged overnight, and then filtered and washed with distilled water for several times until the filtrate became colorless. The wet solid sample, $CTAMnO_4$, was obtained.

### B. Preparation of pyrolusite

Then the wet $CTAMnO_4$ was gelled again by adding distilled water in 45 mL Teflon-lined stainless steel autoclave. The reactions were carried out at 130 °C for two days under autogenous pressure. Hydrothermally treated samples were filtered, washed several times with distilled water and then dried at 70 °C in air. Hydrothermally treated samples exhibited a characteristic XRD pattern of $\gamma$-MnOOH. According to the TG and DTA data, hydrothermally treated samples were heated to 400 °C with a heating speed of 0.5 °C /min, and maintained at that temperature for 2 h. As-synthesized samples were collected, and ground with mortar and pestle in order to study the effect of grinding on the morphology and the FTIR spectrum. Another sample was synthesized by heating $Mn(NO_3)_2$ at 320 °C for 5 h in an electronic furnace.

### C. Characterizations

XRD analysis was carried out to identify the phase of the samples using a Philips X'Pert PRO SUPER X-ray diffractometer with Cu K$\alpha$ radiation monochromated by graphite at 40 kV and 100 mA. Rietveld refinement of the full pattern was carried out in the DBWS-9807a program. Middle infrared spectra were obtained on a Bruke Vector-22 FTIR spectrometer with use of KBr pellets. Far infrared spectra were obtained on a Nicolet NEXUS 870 FTIR spectrometer. The samples were first put into methyl silicone oil and mixed completely. Then the mixture was dispersed on the polyethylene membrane. For each sample, 32 scans were taken with a resolution of 4 $cm^{-1}$. The morphologies of the samples were observed by TEM (Hitachi-H800, 200 kV), high resolution transmission electron Microscopy (HRTEM) (JEOL2000, 200 kV), and SEM (Hitachi X-650). The samples for TEM and HRTEM were prepared by suspending powder ultrasonically in ethanol and pipetting the solution onto carbon coated copper grids.

The X-ray-absorption spectra at Mn *K*-edge for the samples were measured at the beam line of U7C of National Synchrotron Radiation Laboratory (NSRL). The storage ring of NSRL was operated at 0.8 GeV with a maximum current of 160 mA. The hard X-ray beam was from a three-pole superconducting Wiggler with a magnetic field intensity of 6 T. The fixed-exit Si(111) flat double crystals were used as monochromator. The EXAFS (extended X-ray absorption fine structure) spectra were recorded in a transmission mode with ionization chambers filled with $Ar/N_2$ at room temperature, using Keithley Model 6517 Electrometer to collect the electron charge directly. EXAFS data were analyzed by USTCXAFS3 data analysis package compiled by Wan *et al.* according to the standard procedures [20, 21].

## III. RESULTS

### A. Characterizations of XRD and TEM

SEM and TEM images of as-synthesized sample show that the particles are of fibrous shape, their diameters are from 20 nm to 100 nm, and the length is up to several micrometers. Figure 1 (a) and (d) is a typical TEM image, HRTEM (Fig.1(e)) and ED (Fig.1(f)) (electron diffraction) results illustrate that nanofibers grow along *c* axis, which are in excellent agreement with the XRD result (Fig.2(a)). As-synthesized sample is denoted as nanofibers. Nanofibous pyrolusite is fragile, and is eas-

DOI:10.1088/1674-0068/24/02/181-188 

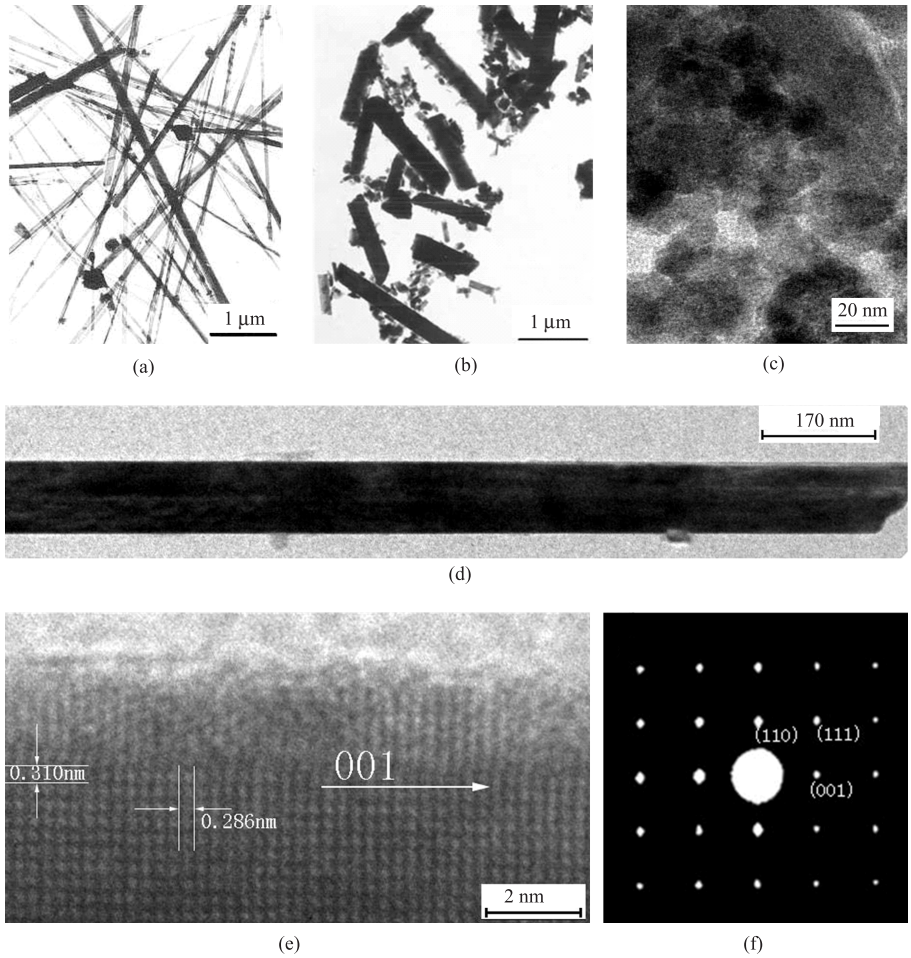


FIG. 1 TEM images of as-synthesized sample (a) and (d), the sample after grinding for 1 h (b), and for 5 h (c). HRTEM image (e) and ED (f) of as-synthesized sample.

ily broken by grinding. Short fibers are formed after grinding for 1 h (Fig.1(b)). Their diameters become larger due to aggregation of fine particles around surface of short fiber. The sample ground for 1 h is denoted short fibers. After grinding for 5 h, nanoparticles are formed, and aggregated together (Fig.1(c)). The sample ground for 5 h is denoted as nanoparticles. Lattice fringes can be clearly observed in HRTEM image, and the sizes of nanoparticles are about a few tens of nanometers.

Figure 2 shows XRD patterns of as-synthesized sample (Fig.2 (a) and (b)) and the samples after grinding for different time (Fig.2 (c) and (d)). Generally speaking, all patterns can be attributed to pyrolusite (JPCDS 24-735). The tiny difference is that the reflection peaks become wider for the ground samples than those for as-synthesized sample. The intensity ratio of (110) reflection and (101) reflection in Fig.2(b) is larger than that of JPCDS 24-735, suggesting that the growth of as-synthesized sample is highly oriented. The result from Fig.2(a) gives a strong support for this point of view. The pattern of Fig.2(a) was recorded from the specimen prepared by dropping the suspension of as-synthesized sample in ethanol on silicon surface. Only the ($hk0$) reflections appear in the pattern, indicating that as-synthesized sample grows perfectly along $c$ axis.

### B. Characterization of FTIR

The FTIR spectra of as-synthesized and ground samples show considerable variation. Figures 3 and 4 are the FTIR spectra in mid- and far-infrared region, respectively. The order of the spectra in Fig.3 is the same as that of the XRD patterns in Fig.2. Figure 3(a) was recorded from the specimen prepared by dropping the suspension of as-synthesized sample in ethanol on KBr crystal surface; others in Fig.3 were obtained from KBr pellet. Figures 3(a) and 4(a) represent the FTIR spectra of nanofibrous pyrolusite because nanofibrous structure can perfectly be kept in the specimen. Otherwise, vibrational bands shift toward higher and lower wavenumber in mid-infrared region for the specimen of KBr pellet (Fig.3(b)). Four vibrational bands in the spectra of nanofibrous pyrolusite are in excel-

DOI:10.1088/1674-0068/24/02/181-188 

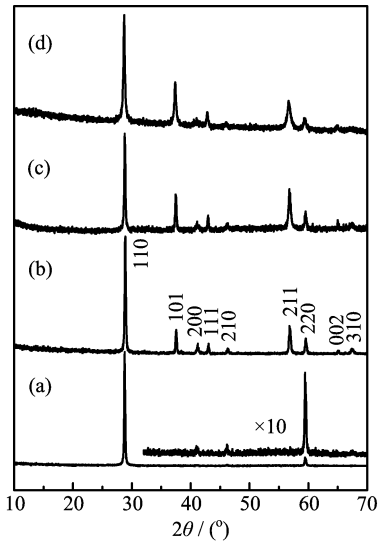


FIG. 2 XRD patterns of as-synthesized sample ((a) and (b)) and the samples after grinding for 1 h (c), 5 h (d).

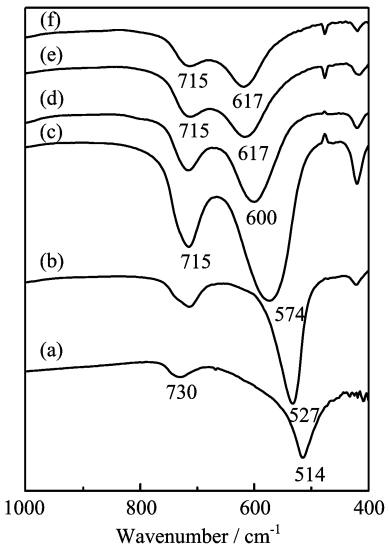


FIG. 3 Middle infrared spectra of as-synthesized samples ((a) and (b)) and the samples after grinding for 1 h (c), 2.5 h (d), 5 h (e), and 8 h (f).

lence agreement with the prediction of the factor group analysis for the tetragonal structure in infrared active modes. These bands are located at 343($\nu_1$), 421($\nu_2$), 514($\nu_3$), and 730 cm$^{-1}$($\nu_4$), respectively. The intensity of $\nu_3$ band is very strong, $\nu_4$ is middle, and $\nu_1$ and $\nu_2$ are very weak. The number of vibrational bands does not change in the FTIR spectra of the ground samples, which is correlated with the XRD patterns since the phase structures do not change (Fig.2). However, three trends are suggested to be going from bottom to top in Fig.3 and Fig.4. The first one is that $\nu_3$ band shifts gradually toward higher wavenumber, and the variation of this band is about 103 cm$^{-1}$. The second one is that

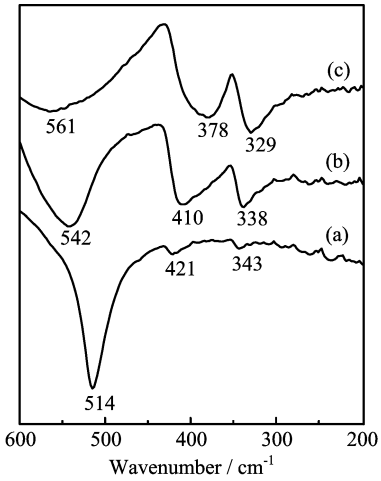


FIG. 4 Far infrared spectra of as-synthesized sample (a) (nanofibers), and the sample after grinding for 1 h (b) (short fibers), and 5 h (c) (nanoparticles).

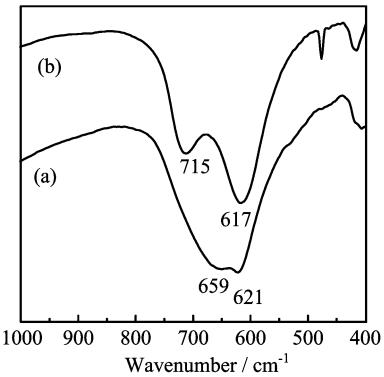


FIG. 5 Middle infrared spectra of pyrolusites synthesized by heating $Mn(NO_3)_2$ at 320 °C for 5 h (a) and by heating $\gamma$-MnOOH at 400 °C for 2 h and then grinding for 5 h (b).

$\nu_1$, $\nu_2$, and $\nu_4$ bands shift toward lower wavenumber, the change observed in this work is about 14 cm$^{-1}$ for $\nu_1$ band, 43 cm$^{-1}$ for $\nu_2$ band, and 15 cm$^{-1}$ for $\nu_4$ band. The third one is that the intensities of $\nu_1$, $\nu_2$, and $\nu_4$ bands grow with respect to $\nu_3$ band.

Figure 5 shows the FTIR spectra of pyrolusites produced by heating $Mn(NO_3)_2$ at 320 °C for 5 h (Fig.5(a)), and heating $\gamma$-MnOOH at 400 °C for 2 h (Fig.5(b)), respectively. In order to avoid the effect of particle shape and size, the samples were ground for enough time until their spectra did not change any more (see Fig.3 (e) and (f)). Actually, little change was observed for the sample made by heating $Mn(NO_3)_2$ before and after grinding. Two vibrational bands present in the middle infrared spectrum for each sample. The obvious difference between two spectra is that the maximum vibrational frequency is different. One is located at 659 cm$^{-1}$ (Fig.5(a)), and another is at 715 cm$^{-1}$ (Fig.5(b)).

DOI:10.1088/1674-0068/24/02/181-188 

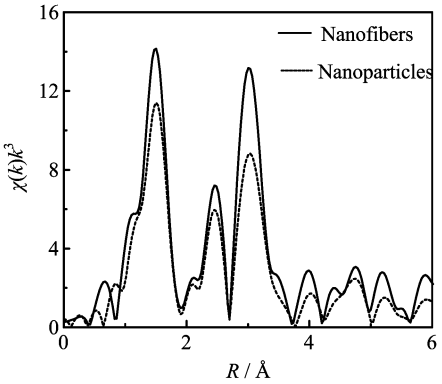


FIG. 6 Fourier transformed experimental Mn $K$-edge $\chi(k)k^3$ functions of as-synthesized sample (nanofibers) and the sample after grinding for 5 h (nanoparticles).

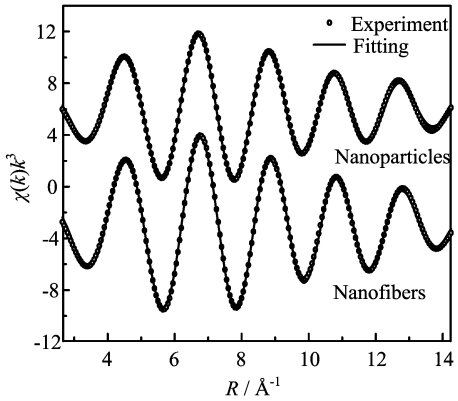


FIG. 7 The curve fitting data for the first peak around 1.5 Å in Fig.6.

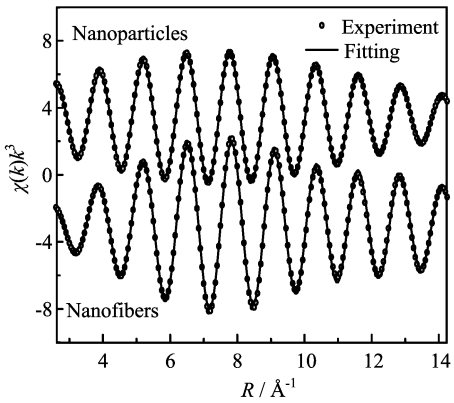


FIG. 8 The curve fitting data for the second peak around 2.5 Å in Fig.6.

TABLE I EXAFS fitting results of nanofibrous and nanoparticle poyrolusite.

| Sample | Pair type | $R$/Å | CN | $\sigma^2$/Å$^2$ |
|---|---|---|---|---|
| Nanofiber | Mn−O | 1.829 | 2 | 0.0022 |
| | Mn−O | 1.901 | 4 | 0.0026 |
| | Mn−Mn | 2.868 | 2 | 0.0074 |
| Nanoparticle | Mn−O | 1.843 | 2 | 0.0032 |
| | Mn−O | 1.909 | 4 | 0.0035 |
| | Mn−Mn | 2.904 | 2 | 0.0095 |
| Ref.[27] | Mn−O | 1.875 | 2 | 0.0022 |
| | Mn−O | 1.902 | 4 | 0.0022 |
| | Mn−Mn | 2.869 | 2 | 0.0025 |

### C. Characterization of EXAFS

XAFS technique has long been recognized as a powerful tool for determining the local structure of condensed matters, because of its sensitivity to the short-range order and atomic species surrounding the absorber [22, 23]. Hence, XAFS may provide further information to those obtained by X-ray or neutron diffraction. The Fourier transform (FT) of the EXAFS oscillation function $\chi(k)k^3$ at the Mn K-edge obtained is shown in Fig.6 for nanofibers and nanoparticles. The first peak around 1.5 Å in the FT spectra corresponds to the Mn-O interaction in $MnO_6$ octahedra, the second one around 2.5 Å is the Mn−Mn interaction which corresponds to $MnO_6$ octahedra linked by edges, and the third one at around 3.0 Å is the Mn−Mn interaction which corresponds to $MnO_6$ octahedra linked by corners [24−26].

To obtain the local structural information of $MnO_2$ nanofibers and nanoparticles quantitatively, the radial structural functions as shown in Fig.6 are inversely transformed to isolate the single shell EXAFS contribution. The least-square curve fit technique, based on Marquart's scheme for iterative estimation of nonlinear least-squares parameters via a combination of gradient and Taylor series method was used to fit the inverse transform EXAFS oscillations. Figures 7 and 8 show the curve-fitting analysis for Mn-O shell and Mn-Mn shell, and Table I summarizes the structural parameters obtained by curve-fitting, where the data from Ref.[27] are included. Fitting errors in distance are estimated to be about 0.03 Å. The Debye-Waller factor for the Mn-O shell in nanoparticles is larger than that in nanofibers, indicating that nanoparticles has more local structural disorder. This is in good agreement with the low peak height in the FT spectrum and the broad XRD reflection.

### D. Rietveld refinement analysis

Rietveld refinement of the full XRD pattern was carried out for nanoparticles and pyrolusite produced by heating $Mn(NO_3)_2$. Unfortunately, the refinement is not suitable for calculating the XRD patterns of nanofibers and short fibers due to high orientation. Figure 9 shows a typical result of Rietveld refinement analysis. The structural parameters obtained by the refinement are listed in Table II. Mn−O interatomic distances obtained by Rietveld refinement are very close to the values obtained by EXAFS analysis for nanoparticles.

DOI:10.1088/1674-0068/24/02/181-188 

TABLE II XRD refinement results of pyrolusite.

| Sample | Lattice parameter/Å | | Oxygen | Mn−O distance/Å | | R-P | R-WP | S | D-WD |
|---|---|---|---|---|---|---|---|---|---|
| | $a$ | $c$ | position | Axial | Equatorial | | | | |
| 1 | 4.4020 | 2.8743 | 0.2907 | 1.8501 | 1.8830 | 3.28 | 4.14 | 1.00 | 1.15 |
| 2 | 4.4006 | 2.8749 | 0.3157 | 1.8935 | 1.8850 | 3.36 | 4.27 | 1.34 | 0.56 |
| 3 | 4.3999 | 2.8740 | 0.3053 | 1.8997 | 1.8796 | | | | |

1: nanoparticles, 2: $\beta$-$MnO_2$ produced by heating manganous nitrate at 320 °C for 5 h, 3: JPCDS 24-735.

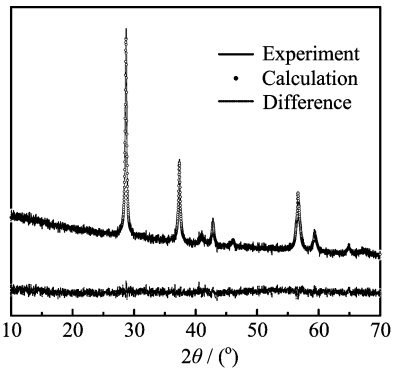


FIG. 9 Observed and calculated (by Rietveld-method) XRD pattern of nanoparticles and the difference between those two patterns.

Both Rietveld refinement and EXAFS results indicate that $MnO_6$ is of 4 long+2 short octahedra geometry in nanoparticles, which is in agreement with the result of Ref.[27]. The relationship between the oxygen position and the ratio of the lattice constants of $c/a$ obtained by Rietveld refinement further confirms 4 long+2 short octahedral geometry [28]. Rietveld refinement result for the sample produced by heating $Mn(NO_3)_2$ indicates that $MnO_6$ is of 2 long+4 short octahedral geometry, which is in agreement with the relationship between the oxygen position and the ratio of the lattice constants of $c/a$ [28], and in agreement with $MnO_6$ octahedral geometry of JCPDS 24-735 (Table II) and Ref.[28].

4 long+2 short and 4 short+2 long octahedral geometries are very common distorted octahedrons in rutile-structural dioxides [28]. The present study suggests that those two geometries could present in pyrolusites synthesized from different route.

## IV. DISCUSSION

### A. The origin of the variation in the FTIR spectra

Although the FTIR spectrum is sensitive to the short-range environment of oxygen coordination around the cation in oxide lattices, the change of the local structure occurring in the samples after grinding can not be used to explain the variations shown in Fig.3 and Fig.4. For example, the increase of Mn−O distance from as-synthesized sample to the ground samples should lead to the shift of vibrational bands toward lower wavenumber, however, the shift of $\nu_3$ band is about 103 $cm^{-1}$ toward higher wavenumber. Alternative explanation may concern the change of the morphology and size, which was found for rutile $TiO_2$ and rutile-structured $SnO_2$ [11−14]. Farmer gave the theoretical explanation [11]. The $A_{2u}$ vibration of rutile $TiO_2$ and rutile-structured $SnO_2$ migrates from its LO frequency (higher wavenumber) to its TO frequency (lower wavenumber) during a transition in crystal shape from platy to needle-like morphology, with $c$ perpendicular to the plates and parallel to the long axes of the needles. At the same time the Eu frequencies migrate from their TO values to their LO values. These are smaller shifts than for the $A_{2u}$ vibration but the bands would show profound changes in relative intensity. These descriptions are in excellent agreement with the variation in FTIR spectra of rutile-structured pyrolusite (Fig.3 and Fig.4), just the change of morphology in this study is from nanofiber to nanoparticle. The conclusion can be made that the variation in the FTIR spectra of pyrolusite can be ascribed to the effect of particle shape and size, similar to the case of $TiO_2$ and $SnO_2$ [11−14]. Following Farmer's assignment [11], $\nu_3$ band can be assigned to the $A_{2u}$ mode, $\nu_1$, $\nu_2$, and $\nu_4$ bands are assigned to $E_u^1$, $E_u^2$, and $E_u^3$ modes, respectively.

### B. The origin of the extra band unpredicted by theory

Due to the large variation of $A_{2u}$ mode with the morphology, two or more $A_{2u}$ mode vibrational bands could present in the FTIR spectrum for the sample containing two or more particle shapes. This assumption was demonstrated by experiment. Nanofibers and nanoparticles were mixed together with the weight ratio of 1:3, and then the mixed sample was pressed into KBr pellet. The FTIR spectrum of the mixed sample is shown in Fig.10. There are three bands in the middle infrared region. Two of them at 527 and 611 $cm^{-1}$ are attributed to $A_{2u}$ mode of nanofibers and nanoparticles, respectively. The present study reveals that the extra band originates from $A_{2u}$ mode vibration from particles with different shapes. The present result can be used to explain the FTIR spectra presented by Nilsen *et al.* [8], Julien *et al.* [7], and Potter and Rossman [6].

DOI:10.1088/1674-0068/24/02/181-188 

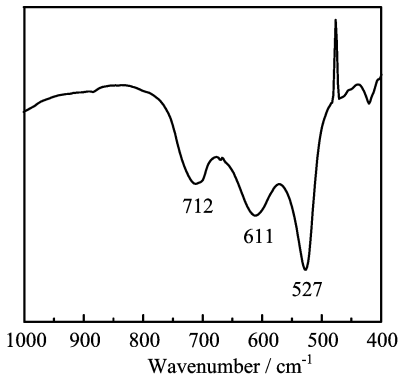


FIG. 10 Middle infrared spectrum of the mixed sample of nanofibers and nanoparticles with the weight ratio of 1/3.

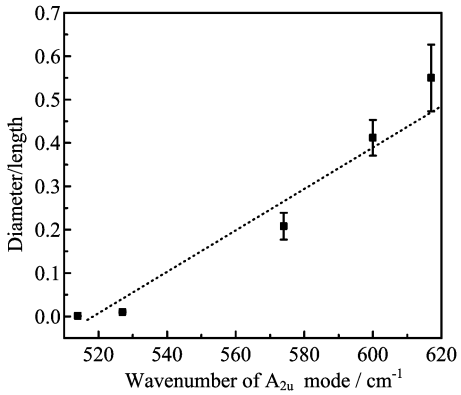


FIG. 11 The relationship between the $A_{2u}$ mode frequency and the diameter/length ratio of particles.

### C. The relationship between $A_{2u}$ mode frequency and the diameter/length ratio of particles

The information from Fig.1 and Fig.3 suggests that there could be a relationship between $A_{2u}$ mode frequency and the diameter/length ratio of particles as shown in Fig.11. This relationship is useful for predicting the particle shape on the basis of the FTIR spectrum. For example, one can estimate that the film of $\beta$-$MnO_2$ is composed of long- and short-fibers since the major bands ($A_{2u}$ modes) are at ∼520 and ∼584 $cm^{-1}$ [8, 29]. Needles of $\beta$-$MnO_2$ with different sizes present in TEM image [29]. The morphology of $\beta$-$MnO_2$ particles made by the reduction of $KMnO_4$ is of short barlike shape [30], whose $A_{2u}$ mode vibrational frequency is 576 $cm^{-1}$.

### D. The origin of the different maximum vibrational frequency

The maximum frequency of pyrolusite in the FTIR spectra seems to be dependent on the sample source and the synthesis route. The different maximum frequency, ∼650 or ∼720 $cm^{-1}$, was observed by experimental measurement. 650 $cm^{-1}$ vibrational band appears in the spectra of $\beta$-$MnO_2$ film [8], $\beta$-$MnO_2$ produced by decomposition of $Mn(NO_3)_2$ [9] and some natural pyrolusite samples [6], whereas the band at about 720 $cm^{-1}$ appears in some natural pyrolusite samples [6], $\beta$-$MnO_2$ from Aldrich [7], and standard powdered sample [8]. These two frequencies were observed in this work from different samples (Fig.5). Some commercial samples (AR grade and spectrum grade, Shanghai, China) show the same spectrum as Fig.5(a). Figure 5(a) is also a repeated result of Ref.[9] since the synthesis route is the same, suggesting that the maximum frequency is indeed dependent on the synthesis route. The variation of the maximum frequency may originate from the change of the micro-structural environment. From Table II, it can be found that the largest difference in pyrolusites made from different route is Mn−O distance along axial direction. According to the symmetries of the $A_{2u}$ and $3E_u$ optic modes of the rutile structure for zero wave vector (Fig.12), the change of the axial Mn−O distance should have a serious effect on $E_u$ mode vibrational frequency, and have a little effect on $A_{2u}$ mode because the $A_{2u}$ species corresponds to a displacement of $Mn^{4+}$ relative to the $O^{2-}$ along $c$-axis (Fig.12(a)), and the three $E_u$ species give dipole oscillations perpendicular to this axis (Fig.12 (b), (c), and (d)). The shorter the axial Mn−O distance is, the higher the vibrational wavenumber of $E_u$ mode is. $A_{2u}$ mode vibrational frequency is not sensitive to the variation of the axial Mn−O distance, indicating that the maximum frequency is very sensitive to the variation of octahedral geometry.

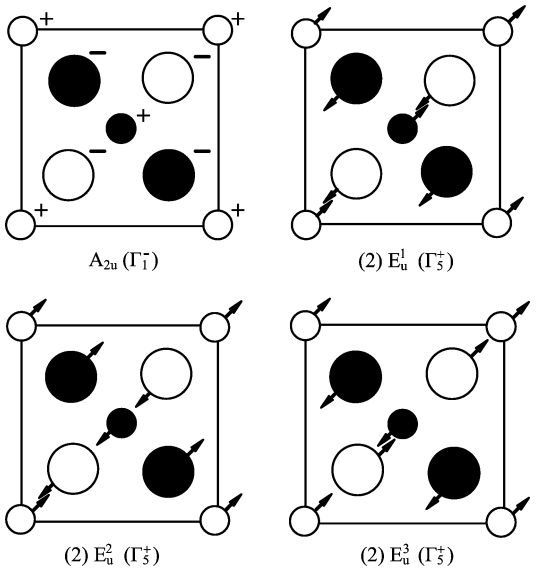


FIG. 12 Symmetry of the $A_{2u}$+$3E_u$ optic modes of the rutile structure for zero wave vector. Labeling is in the notation of Mulliken and, in parentheses, of Koster. Doubly degenerate modes are indicated by a "2" preceding the Mulliken symbol.

DOI:10.1088/1674-0068/24/02/181-188 

## V. CONCLUSION

The extra vibrational band that is unpredicted by factor group analysis originates from the contribution of $A_{2u}$ mode vibration from the particles with different shapes and sizes in the studied sample. The variation in the FTIR spectrum of pyrolusite is ascribed to the change of particle shape and size, similar to other rutile-structural oxides, such as $TiO_2$ and $SnO_2$. The largest variation observed in this work is $A_{2u}$ mode. The particle shape and size change from long nanofibers to short fibers to nanoparticles, $A_{2u}$ mode vibrational frequency shifts from 514 $cm^{-1}$ to 574 $cm^{-1}$ to 617 $cm^{-1}$ gradually. The relationship between $A_{2u}$ mode vibrational frequency and the particle shape and size is useful for estimating the particle shape even though infrared spectroscopy is blind for the particle shape and size. Two kinds of distorted $MnO_6$ octahedral geometries, *i.e.*, 4 long+2 short and 4 short+2 long, could exist in pyrolusites on the basis of the results of Rietveld refinement and the FTIR spectra. The maximum frequency originates from $E_u^3$ mode vibration. This mode vibrational frequency is sensitive to the Mn−O distance along axial direction. The shorter the axial Mn−O bond is, the higher the maximum vibrational frequency is.

## VI. ACKNOWLEDGMENTS

This work was supported by the Education Department of Anhui Province and the measurement and analysis center of Chinese Academy of Science in Hefei.

[1] S. L. Suib, *In Recent Advances and New Horizens in Zeolite Science and Technology*, H. Chon, S. H. Woo, and S. E. Park, Ed., Amsterdam: Elsevier, 102, 47 (1996).
[2] Y. F. Shen, R. P. Zerger, R. N. DeGuzman, S. L. Suib, L. McCurdy, D. I. Potter, and C. L. O'Young, Science **260**, 511 (1993).
[3] M. M. Thackeray, Prog. Solid St. Chem. **25**, 1 (1997).
[4] A. F. Wells, *In Structural Inorganic Chemistry*, 4th Ed., Oxford: Clarendon, 458 (1975).
[5] Y. Chabre and J. Pannetier, Prog. Solid St. Chem. **23**, 1 (1993).
[6] R. M. Potter and G. R. Rossman, Am. Miner. **64**, 1199 (1979).
[7] C. M. Julien, M. Massot, and C. Poinsignon, Spectrochim. Acta **60A**, 689 (2004).
[8] O. Nilsen, H. Fjellvag, and A. Kjekshus, Thin Solid Films **444**, 44 (2003).
[9] W. Tang, X. Yang, Z. Liu, and K. Ooi, J. Mater. Chem. **13**, 2989 (2003).
[10] J. B. Fernandes, B. Desai, and V. N. K. Dalal, Electrochim Acta **28**, 309 (1983).
[11] V. C. Farmer, *In The Infrared Spectra of Minerals*, V. C. Farmer, Ed., London: Mineralogical Society, 183 (1974).
[12] J. T. Luxon and R. Summitt, J. Chem. Phys. **50**, 1366 (1969).
[13] M. Ocana, C. J. Serna, J. V. Garcia-Ramos, and E. Matijevic, Solid State Ionics. **63-65**, 170 (1993).
[14] H. Zhang, Y. Liu, K. Zhu, G. Siu, Y. Xiong, and C. Xiong, J. Phys.: Condens Matter. **10**, 11121 (1998).
[15] D. Zheng, S. Sun, W. Fan, H. Yu, C. Fan, G. Cao, Z. Yin, and X. Song, J. Phys. Chem. B **109**, 16439 (2005).
[16] J. Yuan, K. Laubernds, Q. Zhang, and S. L. Suib, J. Am. Chem. Soc. **125**, 4966 (2003).
[17] X. Wang and Y. Li, J. Am. Chem. Soc. **124**, 2880 (2002).
[18] Z. Liu, W. L. Wang, X. Liu, M. Wu, D. Li, and Z. Zeng, J. Solid State Chem. **177**, 1585 (2004).
[19] W. L. Wang, H. Jiang, Z Liu, and X. Liu, J. Mater. Chem. **15**, 1002 (2005).
[20] X. H. Wan and S. Q. Wei, USTCXAFS Software Package, (1999).
[21] D. E Sayers and B. A Bunker, *In X-ray Absorption, Principles, Applications, Techniques of EXAFS, SEXAFS and XANES*, John Wiley and Sons, Inc., 211 (1998).
[22] S. Wei, H. Oyanagi, K. Sakamoto, Y. Takeda, and T. P. Pearsall, Phys. Rev. B **62**, 1883 (2000).
[23] S. Wei, W. Yan, Y. Li, W. Liu, J. Fan, and X. Zhang, Physica B **305**, 135 (2001).
[24] C. Godart, M. Latroche, C. Fretigny, and C. Levy-Clement, Phys. Stat. Sol. (a) **132**, 253 (1992).
[25] J. B. Li, K. Koumoto, and H. Yanagida, J. Mater. Sci. **23**, 2595 (1988).
[26] A. Manceau, A. I. Gorshkov, and V. A. Drits, Am. Mineralogist. **77**, 1144 (1992).
[27] T. Ressler, S. L. Brock, J. Wong, and S. L. Suib, J. Phys. Chem. B **103**, 6407 (1999).
[28] A. A. Bolzan, C. Fong, B. J. Kennedy, and C. J. Howard, Acta Cryst. B **53**, 373 (1997).
[29] O. Nilsen, S. Foss, H. Fjellvag, and A. Kjekshus, Thin Solid Films **468**, 65 (2004).
[30] W. L. Wang, M. Wu, and X Liu, J. Solid State Chem. **164**, 5 (2002).

DOI:10.1088/1674-0068/24/02/181-188 